Biointerface Research in Applied Chemistry
Open-Access Journal (ISSN: 2069-5837)

Article
Volume 16, Issue 3, 2026, 72
https://doi.org/10.33263/BRIAC163.072

Magnetic and Thermal Behavior of Hydrothermally Synthesized $Bi_{0.2}Ni_{0.8-y}Gd_yFeO_3$ (y=0.2-0.8) Nanorods

Sake Devendra [1,2], L. Siva Sankara Reddy [1*], M. Chandrasekhar [3], D. Baba Basha [4]

[1] Department of Physics, Sri Krishnadevaraya University, Anantapuramu-515003, A.P, India
[2] Department of Physics, Government College (A), Ananthapur -515001, A.P, India; sakedevendra1985@gmail.com;
[3] Dept. of Physics, Chaitanya Bharathi Institute of Technology, Hyderabad-500075; chandrasekharm_physics@cbit.ac.in;
[4] College of Computer and Information Sciences, Majmaah University, Al-Majmaah, K.S.A. 11952; b.dudekula@mu.edu.sa;
* Correspondence: reddy.lss@gmail.com;

Received: 31.03.2026; Accepted: 5.05.2026; Published: 29.05.2026

Abstract: The rare-earth Gd-substituted $Bi_{0.2}Ni_{0.8-y}Gd_yFeO_3$ (BGNFO) nanorods with varying y-content from 0.2, 0.4, 0.6, and 0.8 were prepared using a hydrothermal route. The phase identification confirmed the formation of a trigonal structure as the primary phase, while the secondary phases are associated with $Bi_2Fe_4O_9$. The morphology evidently shows the deformation of microstructure from nanoparticles to nanorods with the increase of Gd-content in the parent perovskite system (BNF). Specifically, the TEM images confirm the clear development of nanorods. The magnetization versus applied magnetic field (M-H) curves demonstrate the apparent formation of a hysteresis loop with little hard magnetic nature of x=0.2-0.8. The magnetization was varied from $12x10^{-3}$ to $26x10^{-3}$ emu in an unsystematic manner as a function of 'y '. The weight loss (Δw) as a function of temperature (30-700°C) and composition is recorded for BNGF samples using a thermogravimetric study. On the other hand, the DSC curves of x=0.2-0.8 provide the transition temperatures between the range 30 to 1400°C. The compositional dependence of structural, magnetic, and thermal properties was investigated in detail.

Keywords: perovskite: nanoparticles; X-ray diffraction; magnetic; thermal.

1. Introduction

It has been noticed that $BiFeO_3$ (BF) materials show the multiferroic perovskite structure with a general chemical formula: $AFeO_3$ (where A is a trivalent cation) [1]. These materials have attracted significant attention owing to their efficient properties, such as multiferroic nature, high dielectric constant, low loss, piezoelectricity, photocatalytic activity, high power density, high energy density, and high density, making them suitable for memory devices, nanocatalysts, capacitors, supercapacitors, and piezoelectric devices [1-4]. In addition, perovskites have extensive applications in solar cell devices, biosensors, actuators, etc. [5-9]. In this context, several scientists have prepared multiferroic bismuth ferrite for various applications.

Celis *et al*. [10] studied the control of multiferroic properties of bismuth ferrite nanoparticles via various approaches. Indriyani *et al*. [11] prepared the bismuth ferrite nanoparticles using one-pot green synthesis, for which the Abelmoschus esculentus L leaves

extracts are utilized. The photocatalytic dye degradation applications were reported. The piezo-photocatalyst nature of bismuth ferrite was illustrated by Ambouni *et al*. [12]. Parvathy *et al*. [13] reported the atomic-scale insights of BF nanoparticles. Parida *et al*. [14] used a different synthesis process called plant extract mediated preparation of BF nanoparticles and showed the photocatalytic degradation of MB dye. Basith *et al*. [15] developed the BF nanoparticles via low-temperature synthesis. Further, the results demonstrated improved magnetization and enhanced photocatalytic performance in dye degradation and hydrogen evolution. The crystal growth mechanisms and the structure evaluation were clearly made by Bai *et al*. [16]. Cheng *et al*. [17], prepared the perovskite BF nanoparticles and revealed the existence of oxygen vacancies for n-Butanol gas sensing applications. Wu *et al*. [18,19] fabricated the BF nanoparticles and reported the enhanced photocatalytic activity via the electrical polarization. The strong pyro-catalysis of the pyroelectric nature of BF under room temperature cold-hot alternations. The tunable bandgap variation is observed in BF nanoparticles and demonstrates the roles of microstrain and oxygen defects [20]. Prince *et al*. [21] reported the effect of annealing temperature on the tuning behavior of structural, optical, and magnetic properties. Magnetic and photocatalytic behavior of BF nanoparticles was investigated by Masoud *et al*. [22].

Patel *et al*. [23] prepared the Gd-doped BF nanowires and reported the phase transition and improvement of coercivity. Guo *et al*. [24] revealed the enhanced photocatalytic activity and high ferromagnetic nature of Gd doped BF nanoparticles. The structure, dielectric behavior, and ferroelectric nature of Gd doped BF samples were studied by Vashisth *et al*. [25]. The effect of Gd^{+3} cations on the BF perovskite system was investigated for magnetic as well as photocatalytic behavior of samples [26] and the mechanism behind the photocatalytic nature of gadolinium-doped bismuth ferrite samples was reported [27]. Sindhu *et al*. [28] reported the structure, microstructure, and magnetic properties of Gd doped BF nanoparticles prepared via an EA chelated solution combustion technique. Further, the ac-electrical conductivity, structure, dielectric, magnetic, and photocatalytic properties of Gd doped BF nanoparticles were reported in the literature [29]. Liu *et al*. [30] prepared the Gd and ZrCo-doped BF nanoparticles, and reported the piezo-photocatalytic degradation ofloxacin. The diode-like nature was noticed in the case of $GdBiFeO_3$ layers in Nb: $SrTiO_3$-BF-Pt [31]. Due to this, the potential barrier increased. Jena *et al*. [32] investigated the effect of Gd doping on ferroelectric, magnetic, and optical properties of Bf nanoparticles. Similarly, the Mn doping effect in $BiGdFeO_3$ on ferroelectric behavior was discussed by preparing the samples through chemical solution deposition [33]. Hossain *et al*. [34] reported the improvement of dielectric behavior upon adding 5 % $GdBiFeO_3$ via 2-8 % of Cr doping into the system. The photocatalytic activity of Gd doped BF was increased as compared to pure BF [35].

Moreover, variety of BF based and their composites such as Gd/Co doped BF [36], Gd doped $BiFeO_3$/g-C_3N_4 composite [37], Gd and Ni co-doped $BiFeO_3$ ferrite/r-GO nanocomposite [38], Gd-doped $BiFeO_3$ crystalline nanofibers [39], Mn/Gd doped bismuth ferrite [40], (Gd, Mn) co-doped $BiFeO_3$ thin film [41], co-doped $BiFeO_3$/MXene (Ti_3C_2) nanohybrids [42], Gd and Ce modified multiferroic $BiFeO_3$ [43], Spin-casted (Gd–Zn) co-doped $BiFeO_3$ thin films [44], Gd-doped $BiFeO_3$ nanoparticles [45], Gd and Sn co-doped $BiFeO_3$ supported on nitrogen doped graphene [46], Gadolinium (Gd) and Nickel (Ni) co-doped $BiFeO_3$ [47], 10% Gd and Ti co-doped $BiFeO_3$ [48], Sol-Gel Gd doped $BiFeO_3$ [49], Sr/Gd/Mn/Co doped $BiFeO_3$ thin films [50], Gd doped $BiFeO_3$ multiferroics [51], nanocrystalline $BiFeO_3$ powder by Gd-doping [52], Gd doped $BiFeO_3$ ceramics [53], (La, Gd)

doped BF [54], ITO/Gd-doped $BiFeO_3$/Au heterostructure [55], Gd and Co doped $BiFeO_3$ [56], rare earth (RE=La, Nd, Sm, Gd) doped $BiFeO_3$ [57], $BiFeO_3$ ceramic co-doped with Eu and Gd [58], (Gd, V) co-doped $BiFeO_3$ thin films [59], Gd doped $BiFeO_3$ [60], gadolinium doping on $BiFeO_3$-$PbZrO_3$ [61], Gd doped $BiFeO_3$ [62], Nd^{3+}/Gd^{3+} co-doped $BiFeO_3$ nanoparticles [63], Gd-doped $BiFeO_3$–$BaTiO_3$ solid solution [64], Au anchored perovskite Gd^{3+}:$BiFeO_3$ nanospheres [65], etc., are prepared and characterized the samples for different applications. It is clearly understood from a vast literature survey that many nano and bulk synthesis techniques were used for BF based nanoparticles. Also, it is noted that the Ni-doped BF or Gd-doped BF samples were studied in detail for various applications. But, research work on Gd-substituted $BiNiFeO_3$ nanoparticles was neither prepared nor characterized using any synthesis technique in a detailed manner. At this juncture, the authors are interested in preparing the $Bi_{0.2}Ni_{0.8-y}Gd_yFeO_3$ (with varying y-content from 0.2, 0.4, 0.6, and 0.8) nanoparticles (BGNFO) via the hydrothermal synthesis method (Figure.1), wherein the low operating temperatures, high crystallinity, less expenditure, less time consumption, etc., are some of the benefits as compared to other synthesis methods [66, 67]. Further, the samples are characterized for structure, morphology, magnetic, and thermal properties.

2. Materials and Methods

For the preparation of $Bi_{0.2}Ni_{0.8-y}Gd_yFeO_3$ (y=0.2-0.8) (BGNFO) nanoparticles, the raw materials in nitrate form such as [$Bi(NO_3)_3.5H_2O$, ≥99.99 % purity, Sigma-Aldrich], Nickel (II) nitrate hexahydrate [$Ni(NO_3)_2.6H_2O$, 99.92 % purity, Sigma-Aldrich], Gadolinium (III) nitrate hexahydrate [$Gd(NO_3)_3.6H_2O$, 99 % purity, Sigma-Aldrich] and Iron (III) nitrate nonahydrate [$Fe(NO_3)_3.9H_2O$, 99.99 % purity, Sigma-Aldrich] are selected.

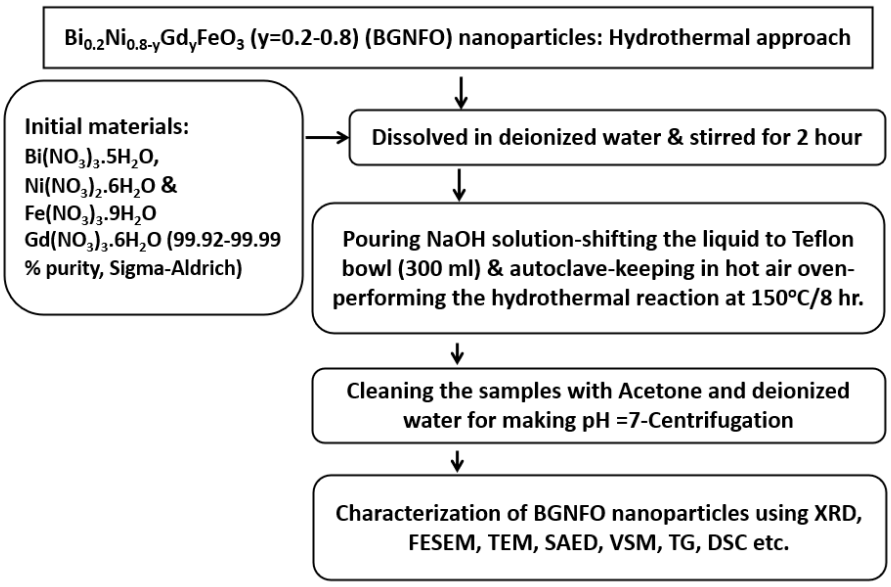

Figure 1. Schematic diagram for the synthesis of $Bi_{0.2}Ni_{0.8-y}Gd_yFeO_3$ (y=0.2-0.8) nanoparticles.

Firstly, these materials were dissolved in the distilled water in a 1:4 ratio. Further, the solution is stirred for two hours constantly with a stirring rate of 550 rpm. In the meantime, the NaOH solution (1:3 ratio) was poured drop by drop into the precursor solution. Then the solution was shifted to a Teflon bowl of 300 mL and then inserted into a stainless steel autoclave. Then the hydrothermal reaction was performed at 150°C for 8 hours. After completion of the reaction, the sample was extracted and washed almost ten times to maintain

a neutral pH. In the next step, the sample was dried/centrifuged to remove the moisture content. The samples in powder and pellet form were sent for various characterizations with the help of the X-ray diffractometer (Bruker XRD, wavelength of $Cu_{K\alpha}$=0.15406 nm), Field-emission scanning electron microscopy (Ultra 55 FE-SEM, Carl Zeiss), Transmission electron microscopy (TEM, Model JEOL JEM 2100), vibrating sample magnetometer, TG-DSC (thermogravimetry-differential scanning calorimetry), etc., for studying the structure, microstructure, magnetic behavior, thermogravimetric analysis, etc., of samples (Figure 1).

3. Results and Discussion

The X-ray powder diffraction patterns are depicted in Figure 2. It is evident that the as-synthesized BGNFO nanoparticles reveal the high crystalline phases at the (104) reflection plane. The peals are on par with the standard JCPDS:71-2494 of bismuth ferrite, including some secondary phases which are connected to $Bi_2Fe_4O_9$ (indexed by * symbol) (JCPDS file No:25-0090). The comparison of current peaks with JCPDS indicated that the samples showed rhombohedral (trigonal) structure. The secondary phases are formed owing to the substitution of Gd^{+3} cations into the bismuth nickel ferrite system. This manner can, in turn, change the unit cell dimensions as reported in literature [68]. According to Shannon [69], it is noted that ionic radii of Bi^{3+}: 0.096 nm, Ni^{2+}: 0.072 nm, Fe^{3+}: 0.064 nm, Gd^{+3}: 0.0938 nm, and Fe^{2+}: 0.063 nm. From this data, one can understand that the ionic radius of Gd^{+3} is much larger than that of Ni^{+2}. The difference is almost 20 %, and therefore, it enhances the fluctuation of the site, leading to an unstable nature of the system. In addition, the valency mismatch shows the problem for charge neutrality. At this moment, the high probability will be there for trivalent cations (Gd^{+3}) to replace the ferric ions or Bi^{+3} cations. This kind of trend usually expands the unit cell volume, thereby increasing the lattice site. It is also understood that, due to a mismatch in charge and ionic radii, the evolution of secondary will occur [68]. Further, it leads to the unsystematic variation of lattice parameters in the compound as a function of composition. In the current work, the Gd^{3+} cations randomly replace either Fe^{+3} cations or Bi^{+3} cations. If it replaces the Bi^{+3} cations, the resultant lattice constant will be increased due to having high ionic radii of Bi^{+3} ions as compared to the Gd^{+3} cations. On the other hand, the gadolinium cations may occupy the ferric ions, inducing a reduction in the lattice constant. However, the occupancy by the gadolinium cations is unpredictable, and it takes place randomly. Consequently, the non-monotonic variation of unit cell dimensions (a, b, and c) as a function of ‘y ’ can be expected here. On par with the expectation, the lattice constants (a, b, and c) are found to be increasing from 0.5628 to 0.5693 nm for y=0.2-0.4, while for y=0.4-0.6, they were decreased from 0.5693 to 0.5648 nm. But for y=0.6-0.8, it is noted to be increasing from 0.5648-0.5702 nm. This kind of trend was earlier reported in the literature [68]. Likewise, the unit cell volume (V) varied nonmonotonically between 440.8 and 453.2 $Å^3$. The Scherrer formula: $D=0.9\lambda/\beta Cos\theta$, where ‘β’ is the full width half maxima, ‘λ’ is the wavelength of CuKα (0.15416 nm), and ‘θ’ is the diffraction angle [69] was used to determine the crystallite size and the results were found to be altering unsystematically between 24.9 to 52.5 nm within the provided error bar limits (Table 1). The reason could be the nonmonotonic variation trend of full width half maxima (FWHM) with the increase of Gd-content. It is seen from Table 1 that the FWHM values are changing from 0.562 to 0.787 radian. This usually offers an inverse proportional relationship with D-value [70-74]. The theoretical density:

$$\rho_x=(Z*CMW)/(N*V) \quad (1)$$

Where Z is the effective number of atoms per unit cell for a trigonal structure, CMW is the compositional molecular weight, and 'N' is Avogadro's number) was evaluated and noted to be increasing from 7.982 to 9.983 g/c.c as a function of Gd-content. The samples became denser owing to the substitution of the Gd element. However, the increasing trend of density took place due to the increase of compositional molecular weight (CMW) from 212.31-271.45 g/mole for y=0.2-0.8. In this sequence, the specific surface area (S) was found to vary unsystematically from 11.4-28.3 m^2/g. Moreover, the variation is inverse to the variation of D.

$$S=6000/(\rho_x*D) \quad (2)$$

In Figure 3, the FESEM images are shown at a 1-micrometer scale and 25 k magnification. The morphology confirmed that the y=0.2 and 0.4 samples clearly showed the spherical and homogeneous nature of the grains. But on the other hand, the y=0.6 sample showed a huge amount of nanorods, and y=0.8 revealed the presence of nanorods hidden among the nanospheres. This kind of morphology deformation happened owing to the presence of Gd^{+3} cations in the BNF system. This can be ascribed to the formation of secondary phases due to ionic radii and valency mismatch as reported in the literature [73, 75]. According to the nucleation process, the doped/substituted cations will induce the oscillations or vibrations due to the developed microstrain. These vibrations will be set up in different orientations of 360°. Hence, the resultant morphological structure will be elongated in that direction, leading to the formation of nanorods that lack flexibility. The grain size was determined using the linear intercept method, which is used to find the average grain size (G_a). For this, the equation: 1.5L/MN, where the L: test line's length, M: magnification & N: the count of the grains intersecting the test line [76-78]. The obtained results concluded that the G_a values vary (86-149 nm) on par with the D-values. But the magnitude of G_a seemed to be very high compared to the crystallite size. In Figure 4, the TEM and SAED images are shown, indicating that the y=0.2 and 0.4 samples exhibit spherical nanoparticles, whereas the y=0.6 and 0.8 samples exhibit nanorod-like microstructures. Clearly, the microstructural deformation is found in the TEM. The results are on par with the FESEM images in terms of shape and deformation as a function of 'y '. The SAED (selected area electron diffraction) patterns explicitly convey that the high intensity was formed for all concentric rings, stating the high crystalline phases of BGNFO. All these rings are on par with the reflection planes of XRD patterns. A little agglomeration was also identified for all the samples when looking at the connected nature of particles/rods due to magnetic interactions among nanostructures [79, 80].

Table 1. Data of structural and physical parameters of $Bi_{0.2}Ni_{0.8-y}Gd_yFeO_3$ (y=0.2-0.8) nanoparticles.

y	0.2	0.4	0.6	0.8
D (nm)	38.2±0.261	24.9±0.528	42.1±0.472	52.5±0.851
a=b (Å)	5.628	5.693	5.648	5.702
c (Å)	13.942	13.986	13.820	13.886
FWHM (β)	0.638	0.787	0.618	0.562
V ($Å^3$)	441.604	453.290	440.857	451.473
CMW (g/mole)	212.31	232.02	251.73	271.45
ρ_t (g/c.c.)	7.982	8.498	9.481	9.983
S (m^2/g)	19.68	28.36	15.03	11.45
G_a (nm)	108	86	127	149

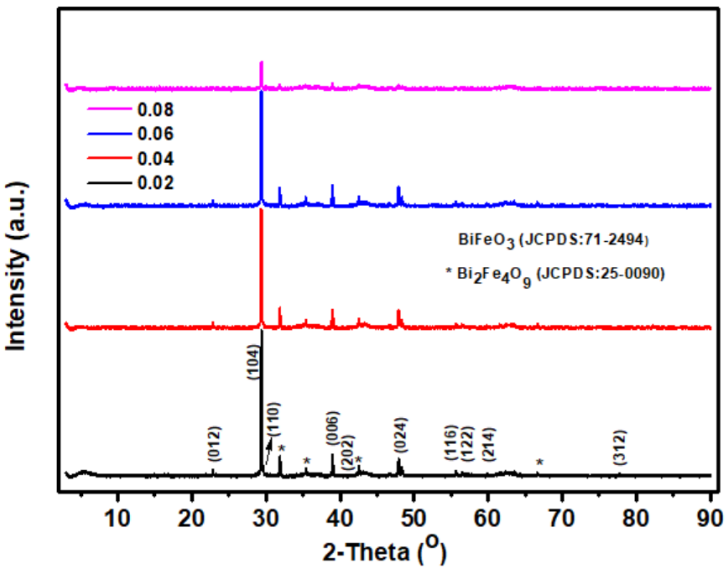

Figure 2. The XRD patterns of $Bi_{0.2}Ni_{0.8-y}Gd_yFeO_3$ (y=0.2-0.8) nanoparticles.

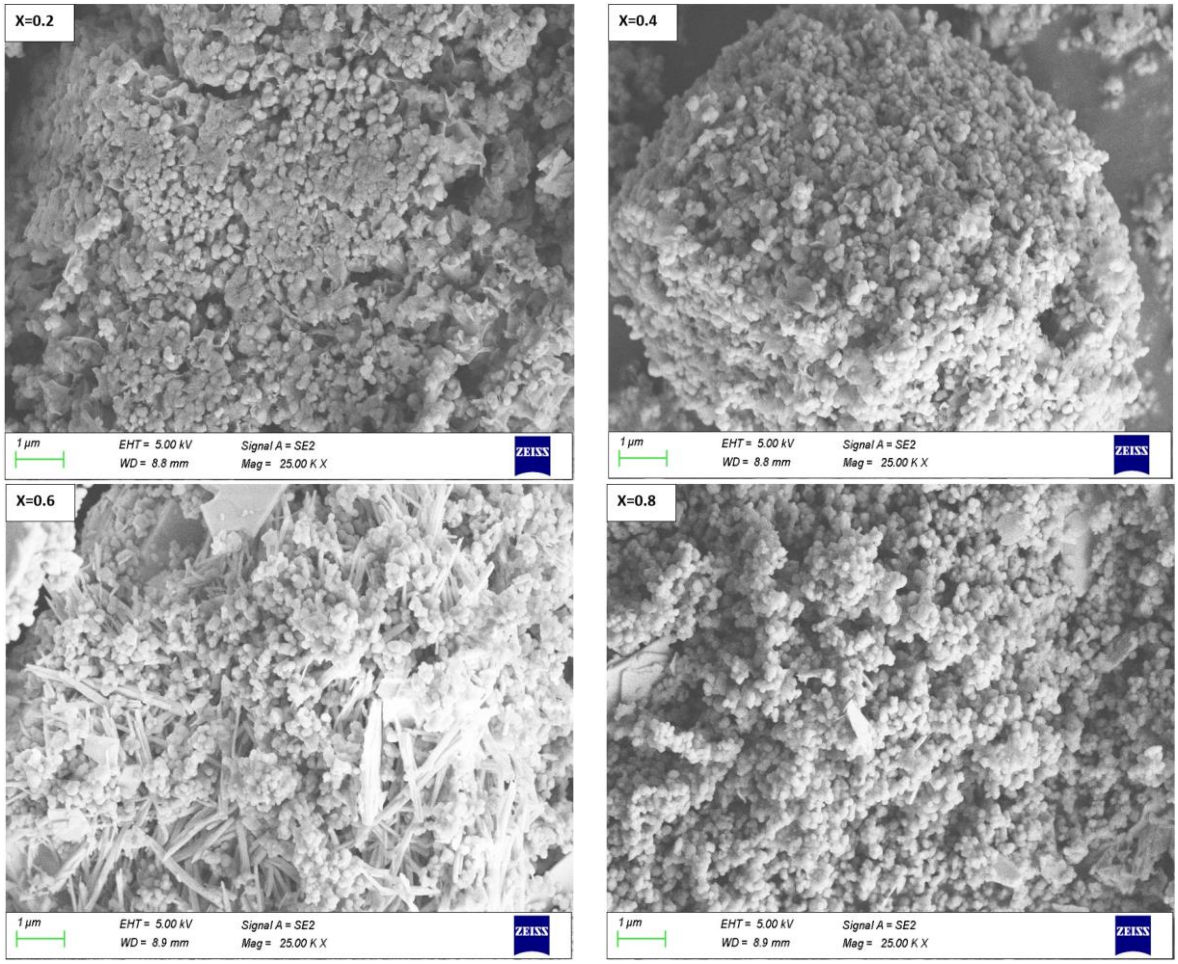

Figure 3. The FESEM images of $Bi_{0.2}Ni_{0.8-y}Gd_yFeO_3$ (y=0.2-0.8) nanoparticles.

The magnetization versus magnetic field curves (M-H) of BGNFO nanorods are shown in Figure 5. It is obvious that the M-H curves are not fully saturated, and they exhibit the unsaturation trend at even the higher magnetic fields. This ensures the existence of paramagnetic content in the y=0.2-0.8 samples. It can be attributed to the presence of Gd and O elements in the system. The M-H curves show the high saturation (maximum) magnetization (M_s/M_{max}) as listed in Table 2. The variation trend depicts the unsystematic manner of magnetization as a function of 'y ' from $12x10^{-3}$ to $26x10^{-3}$ emu (Table 2).

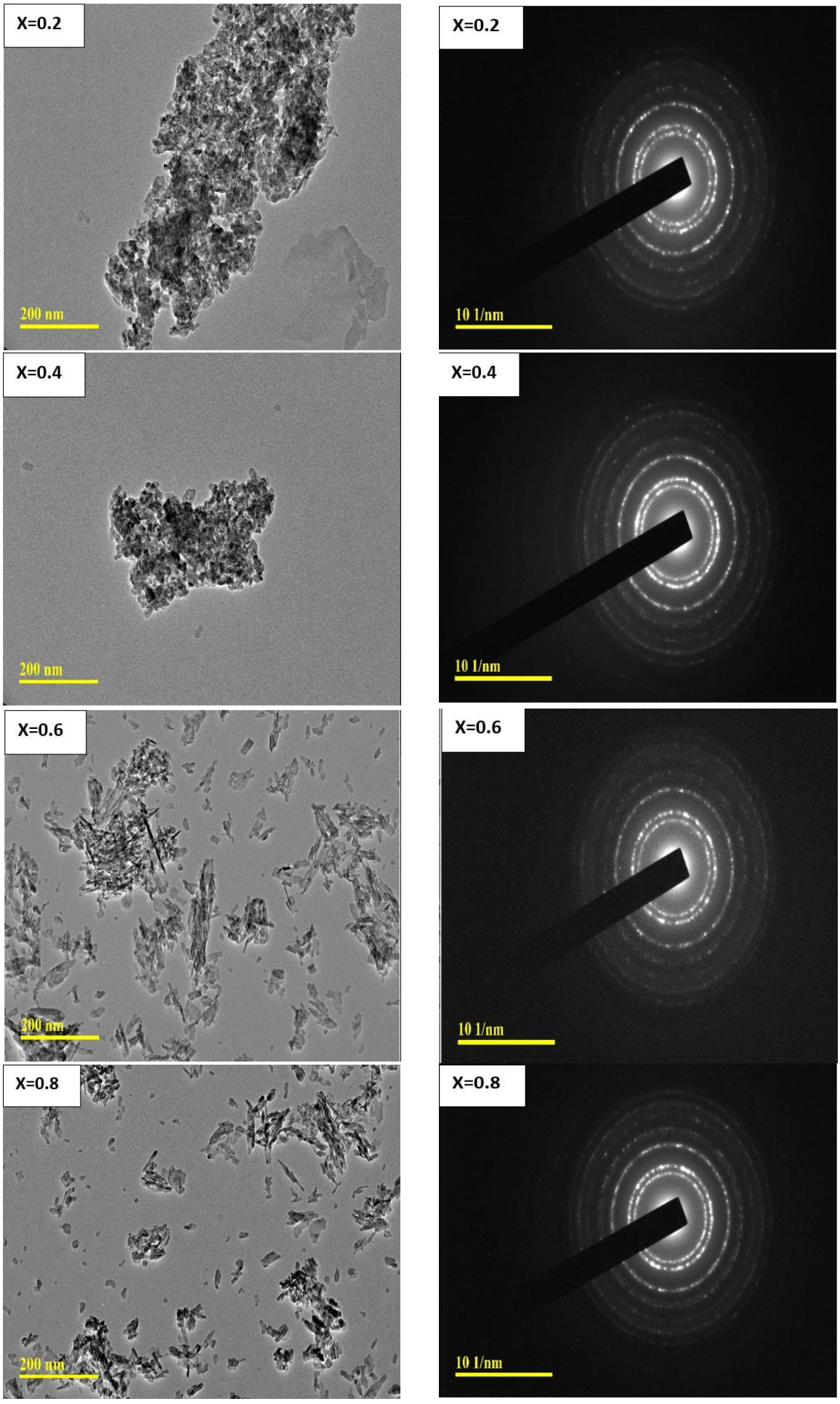

Figure 4. The TEM images and SAED patterns of $Bi_{0.2}Ni_{0.8-y}Gd_yFeO_3$ (y=0.2-0.8) nanoparticles.

The developed secondary phases, as well as paramagnetic content, will usually reduce the magnetization values. The magnetic exchange interactions among Fe-O-Fe vary unsystematically, and therefore, the saturation magnetization values are getting reduced from $12x10^{-3}$ to $26x10^{-3}$ emu with an increase in Gd-content.

The formed ferric ions at the B-site of the perovskite system and even migration of those cations to the A-site may induce the reduction of magnetization with Gd-content [80]. On the other hand, the coercivity H_c also seemed to be high, indicating the hard magnetic nature of the samples. This nature is obtained due to the inclusion of the rare-earth element Gd. The values are altering nonmonotonically with an increase in 'y ' from 785 to 820 Oe. The maximum amount of coercivity is developed due to the domain wall rotation rather than the domain wall displacement.

Table 2. The magnetic parameters of $Bi_{0.2}Ni_{0.8-y}Gd_yFeO_3$ (y=0.2-0.8) nanoparticles.

y	M_s (emu)	H_c (Oe.)	M_r (emu)	$R=M_r/M_s$
0.2	$26x10^{-3}$	820.6	$5.1x10^{-3}$	0.196
0.4	$13x10^{-3}$	785.2	$4.4x10^{-3}$	0.338
0.6	$14x10^{-3}$	800.4	$4.3x10^{-3}$	0.307
0.8	$12x10^{-3}$	801.6	$4.1x10^{-3}$	0.342

Table 3. The thermal parameters (TG-DSC) of $Bi_{0.2}Ni_{0.8-y}Gd_yFeO_3$ (y=0.2-0.8) nanoparticles.

y	Δw (%)	T_g (°C)	T_c (°C)	T_m (°C)
0.2	2.3	200	435	1340
0.4	3.4	205	390	1340
0.6	3.3	200	430	1340
0.8	2.6	195	650	1340

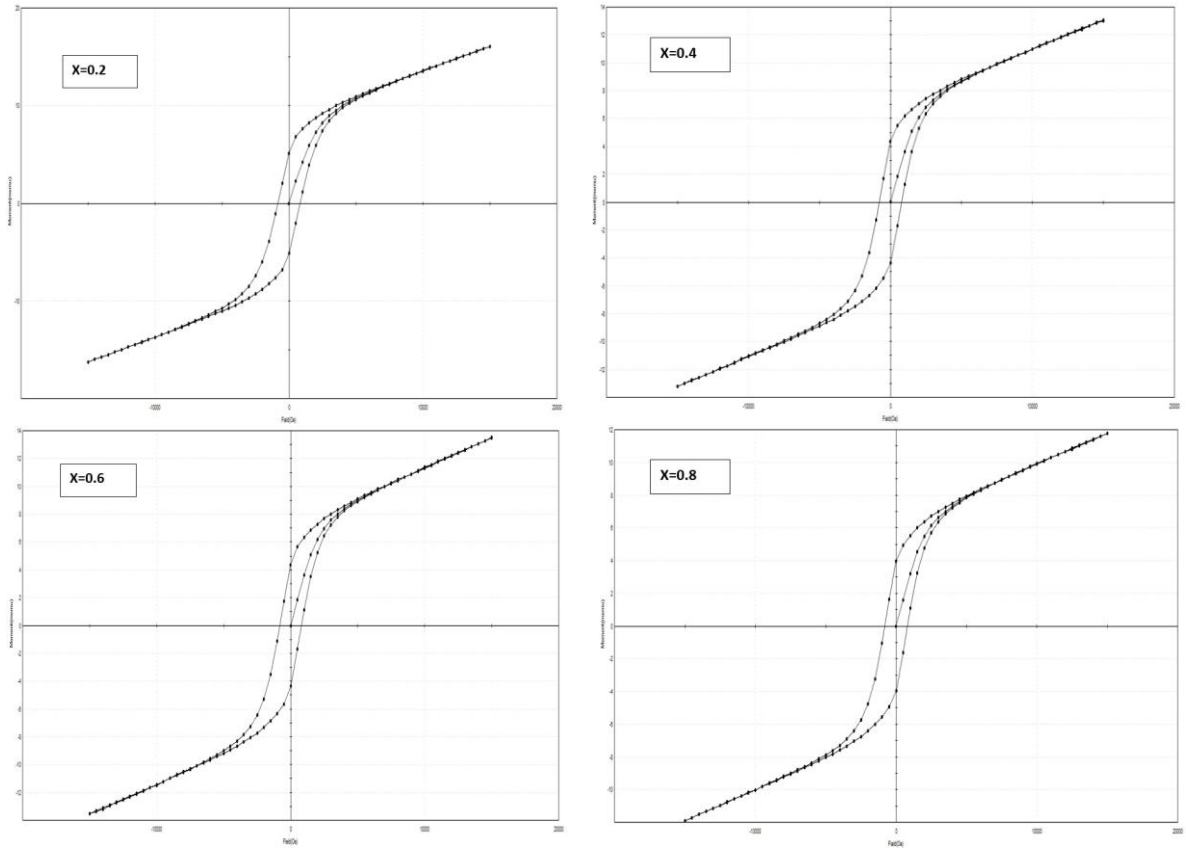

Figure 5. The M-H curves of $Bi_{0.2}Ni_{0.8-y}Gd_yFeO_3$ (y=0.2-0.8) nanoparticles.

The retentivity M_r values are observed to be small, decreasing from $5.1x10^{-3}$ to $4.1x10^{-3}$ emu with an increase in Gd-content. In addition, the squareness ratio R is noted to be less

than 0.5 for all samples. This establishes the fact that the prepared BGNFO nanorods are of multidomain magnetic in nature. The R-values are noted as changing from 0.196 to 0.342. As a whole, it is understood that the samples reveal the ferromagnetic nature pertaining to the paramagnetic terms. A similar kind of observation was noticed in the literature [80].

The TG-DSC curves for BGNFO nanorods are recorded between RT and 700°C and 1400°C, respectively. The TG curves are shown in Figure 6, and Figure 7 shows the DSC curves. The magnitude of some parameters like weight loss (Δw (%)), glass transition T_g (^oC), crystallization T_g (^oC), and melting temperatures T_g (°C) are recorded in Table 3. For y=0.2 and 0.8 samples, the weight loss was found to be less than 2.3 and 2.6 %, respectively. On the other hand, the y=0.4 and 0.6 samples expressed the high weight loss (3.4 and 3.3 %), indicating the high shrinkage of the samples. This ensures that the moisture content and other nitrate products were extracted predominantly from the samples. In the DSC curves, the glass transition temperatures were almost identical at around 200°C, indicating a magnetic transition from ferro to paramagnetic. Above the T_g value, the crystal grains will be formed, showing the conducting region as well as the nonconducting region called the grain boundary. Forming the crystal grains will be referred to as the crystallization process. It happened for all the samples, 400-435°C, except for y=0.8. For y=0.8, the high crystallization temperature (T_c=650°C) was found. This can be attributed to the high grain size/particle size/crystallite size of the sample. In Table 1, the y=0.8 expresses the grain size of 149 nm, and the crystallite size of 52 nm. The sample with high grain size will consume much higher temperatures to be crystallized as well. This temperature even predicts the formation of BGNFO compounds. The diffusion of elements into the structural system will take place at T_c. Similar observations were found in the literature [81, 82]. Above this temperature, gradually the sample gets converted into a liquid and reaches the melting temperature. For y=0.2-0.8 samples, the melting temperatures T_m were noted to be almost equal at 1340°C. This establishes the fact that the Ni-content did not influence the melting temperature. But nevertheless, the Gd content only influenced the melting temperature.

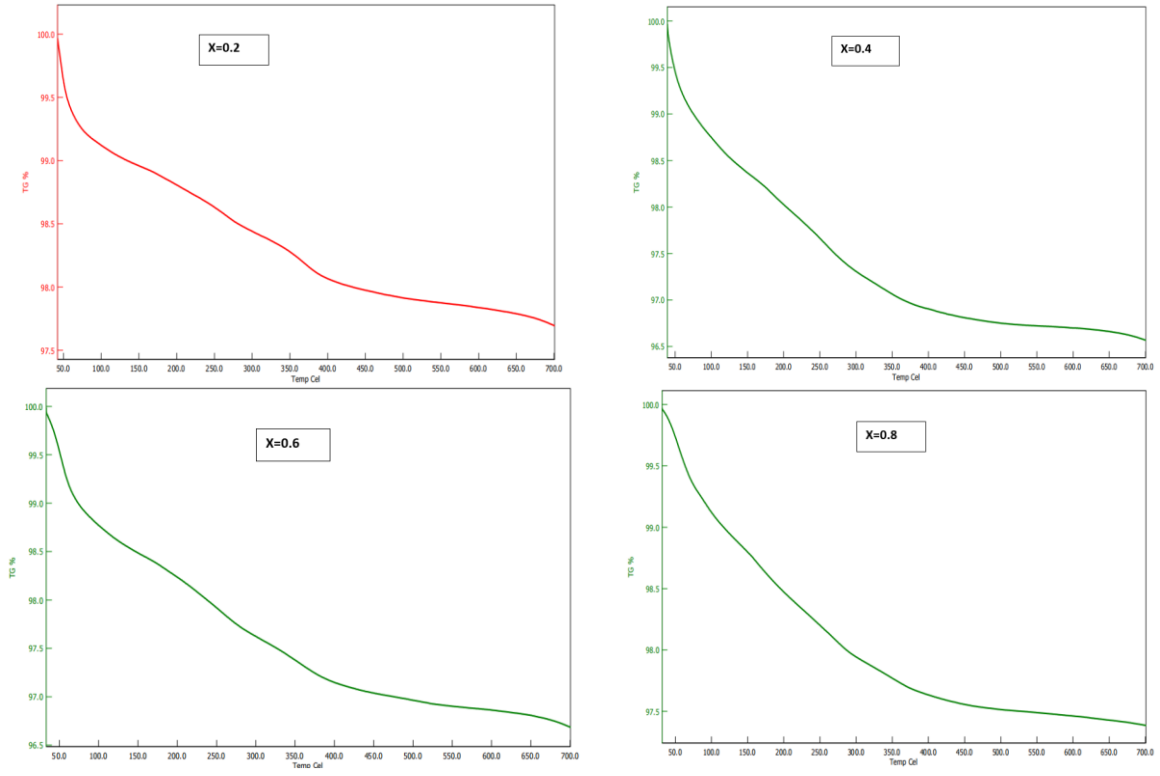

Figure 6. The TG curves of $Bi_{0.2}Ni_{0.8-y}Gd_yFeO_3$ (y=0.2-0.8) nanoparticles.

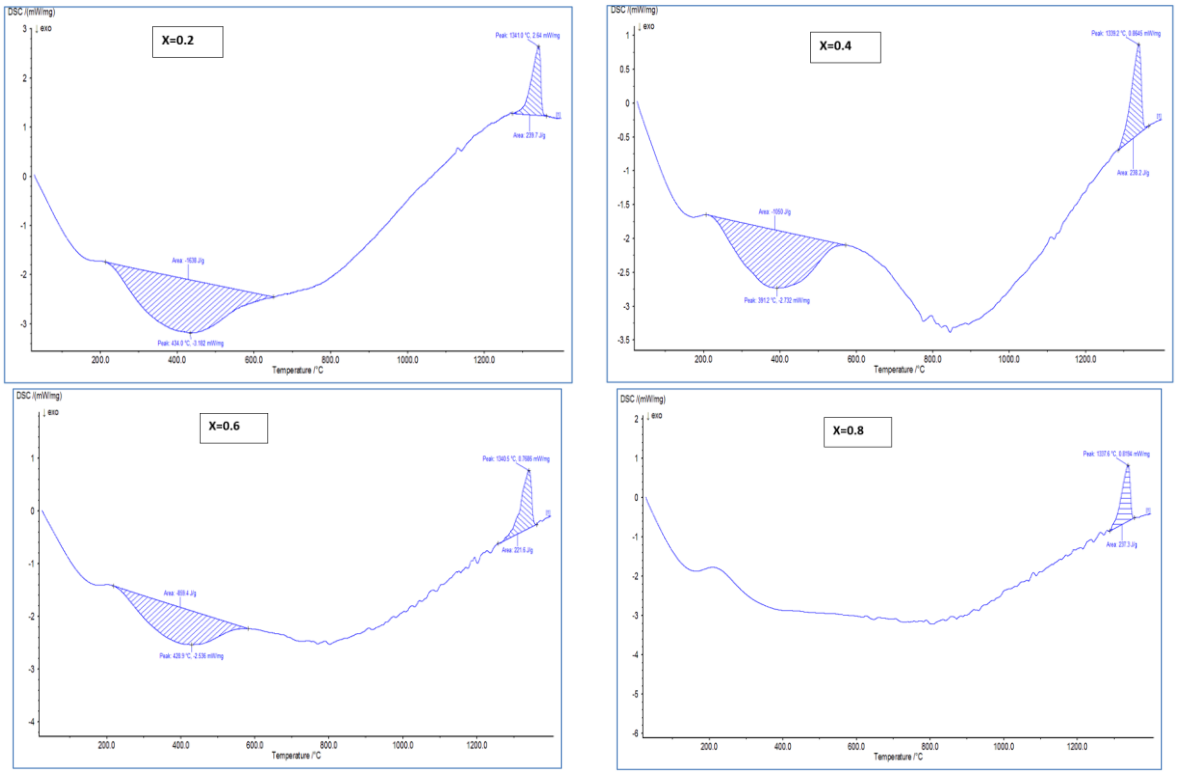

Figure 7. The DSC curves of $Bi_{0.2}Ni_{0.8-y}Gd_yFeO_3$ (y=0.2-0.8) nanoparticles.

4. Conclusions

The BGNFO nanorods were synthesized using a low-temperature hydrothermal route. The XRD analysis confirmed the rhombohedral structure of the samples, including secondary phases. The lattice constants (a, b, and c) are found to be increasing from 0.5628 to 0.5693 nm for y=0.2-0.4, while for y=0.4-0.6, they were decreased from 0.5693 to 0.5648 nm. But for y=0.6-0.8, it is noted to be increasing from 0.5648-0.5702 nm. The FESEM and TEM evidence the formation of nanospheres for y=0.2 and 0.4, while for y=0.6 and 0.8, clearly, the nanorods were formed due to the nucleation process. The high grain size/particle size/ crystallite size was found for the y=0.8 sample. The M-H curves show a ferromagnetic nature with the inclusion of a paramagnetic term (hard magnetic nature). For y=0.2 and 0.8 samples, the weight loss (Δw) was found to be less than 2.3 and 2.6 %, respectively. On the other hand, the y=0.4 and 0.6 samples expressed the high weight loss (3.4 and 3.3 %), indicating the high shrinkage of the samples. The crystallization for all the samples occurred at 400-435°C except for y=0.8. For y=0.8, the high crystallization temperature (T_c=650°C) was found, indicating the high grain size/particle size/crystallite size of the sample. The melting temperature for y=0.2-0.8 samples was recorded at around (T_m) 1340°C. The structure, magnetic nature, and thermal properties are studied in a detailed manner for $Bi_{0.2}Ni_{0.8-y}Gd_yFeO_3$ (y=0.2-0.8) nanoparticles.

Author Contributions

Conceptualization, S.D. and M.S.C.; methodology, S.D.; software, D.B.B.; validation, L.S.S.R.; formal analysis, S.D.; investigation, S.D.; resources, L.S.S.R.; data curation, D.B.B. and M.S.C.; writing—original draft preparation, S.D.; writing—review and editing, L.S.S.R.; visualization, D.B.B. and M.S.C.; supervision, L.S.S.R.; project administration, L.S.S.R.; funding acquisition, L.S.S.R. All authors have read and agreed to the published version of the manuscript.

Institutional Review Board Statement

Not applicable.

Informed Consent Statement

Not applicable.

Data Availability Statement

Data supporting the findings of this study are available upon reasonable request from the corresponding author.

Funding

Not applicable.

Acknowledgments

The authors express thanks to STIC-Kerala, IISC-Bangalore, IIT-Madras, and JNTUA for providing characterizations.

Conflicts of Interest

The authors declare that they have no conflicts of interest.

References

1. Sharma, S.; Mahadevan, S.; Pandey, K.; Singh, P.; Chauhan, S.; Kumar, M.; Siqueiros, J.M.; Herrera, O.R. Phase transition driven enhancements of multiferroic properties in doped $BiFeO_3$: A comprehensive review. *Mater. Sci. Semicond. Process.* **2025**, *195*, 109613, https://doi.org/10.1016/j.mssp.2025.109613.
2. Mitzi, D.B. Introduction: Perovskites. *Chem. Rev.* **2019**, *119*, 3033–3035, https://doi.org/10.1021/acs.chemrev.8b00800.
3. Liu, H.; Yang, X. A brief review on perovskite multiferroics. *Ferroelectrics* **2017**, *507*, 69–85, https://doi.org/10.1080/00150193.2017.1283171.
4. Korde, V.B.; Khot, S.; Kamble, D.B.; Amalraj, S. Review: Perovskite nanostructures materials versatile platform for advance biosensor applications. *Sens. Actuators Rep.* **2024**, *7*, 100201, https://doi.org/10.1016/j.snr.2024.100201.
5. Yin, Y.; Li, Q. A review on all-perovskite multiferroic tunnel junctions. *J. Mater.* **2017**, *3*, 245–254, https://doi.org/10.1016/j.jmat.2017.09.001.
6. Suresh Kumar, N.; Chandra Babu Naidu, K. A review on perovskite solar cells (PSCs), materials and applications. *J. Mater.* **2021**, *7*, 940-956, https://doi.org/10.1016/j.jmat.2021.04.002.
7. Kharbanda, S.; Dhanda, N.; Aidan Sun, A.-C.; Thakur, A.; Thakur, P. Multiferroic perovskite bismuth ferrite nanostructures: A review on synthesis and applications. *J. Magn. Magn. Mater.* **2023**, *572*, 170569, https://doi.org/10.1016/j.jmmm.2023.170569.
8. Verma, K.C.; Kotnala, R.K.; Goyal, N. Multiferroic Systems of $BiFeO_3$ and $BaTiO_3$ Nanostructures: New Ideas and Insights from Recent Magnetoelectric Advancements. In Nanostructured Multiferroics; Balakrishnan, R., Visakh, P.M., Eds.; Wiley: **2021**; pp. 95-132, https://doi.org/10.1002/9783527809967.ch5.
9. Visakh, P.M. Preparations, Characterization, and Applications of Multiferroic Nanocomposites. In Nanostructured Multiferroics; Balakrishnan, R., Visakh, P.M., Eds.; Wiley: **2021**; pp. 233-247, https://doi.org/10.1002/9783527809967.ch9.
10. Carranza-Celis, D.; Cardona-Rodríguez, A.; Narváez, J.; Moscoso-Londono, O.; Muraca, D.; Knobel, M.; Ornelas-Soto, N.; Reiber, A.; Ramírez, J.G. Control of Multiferroic properties in $BiFeO_3$ nanoparticles. *Sci. Rep.* **2019**, *9*, 3182, https://doi.org/10.1038/s41598-019-39517-3.

11. Indriyani, A.; Yulizar, Y.; Tri Yunarti, R.; Oky Bagus Apriandanu, D.; Marcony Surya, R. One-pot green fabrication of $BiFeO_3$ nanoparticles via *Abelmoschus esculentus* L. leaves extracts for photocatalytic dye degradation. *Appl. Surf. Sci.* **2021**, *563*, 150113, https://doi.org/10.1016/j.apsusc.2021.150113.
12. Amdouni, W.; Fricaudet, M.; Otoničar, M.; Garcia, V.; Fusil, S.; Kreisel, J.; Maghraoui-Meherzi, H.; Dkhil, B. $BiFeO_3$ Nanoparticles: The "Holy-Grail" of Piezo-Photocatalysts? *Adv. Mater.* **2023**, *35*, 2301841, https://doi.org/10.1002/adma.202301841.
13. Parvathy, N.S.; Govindaraj, R. Atomic scale insights on the growth of $BiFeO_3$ nanoparticles. *Sci. Rep.* **2022**, *12*, 4758, https://doi.org/10.1038/s41598-022-08687-y.
14. Parida, S.; Nanda, J.; Sarangi, B.; Behera, R. Plant extract mediated synthesis of $BiFeO_3$ nanoparticles for photocatalytic degradation of methylene blue dye. *Biomass Conv. Bioref.* **2025**, *15*, 11607-11622, https://doi.org/10.1007/s13399-024-06100-4.
15. Basith, M.A.; Yesmin, N.; Hossain, R. Low temperature synthesis of $BiFeO_3$ nanoparticles with enhanced magnetization and promising photocatalytic performance in dye degradation and hydrogen evolution. *RSC Adv.* **2018**, *8*, 29613-29627, https://doi.org/10.1039/c8ra04599b.
16. Bai, X.; Bugnet, M.; Frontera, C.; Gemeiner, P.; Guillot, J.; Lenoble, D.; Infante, I.C. Crystal Growth Mechanisms of $BiFeO_3$ Nanoparticles. *Inorg. Chem.* **2019**, *58*, 11364-11371, https://doi.org/10.1021/acs.inorgchem.9b00461.
17. Cheng, Z.; Zhu, H.; Ji, H.; Yuan, Z.; Meng, F. Perovskite-Structured $BiFeO_3$ Nanoparticles with Abundant Oxygen Vacancies for Selective *n*-Butanol Gas Sensing. *ACS Appl. Nano Mater.* **2023**, *6*, 23370-23380, https://doi.org/10.1021/acsanm.3c04754.
18. Wu, J.-Y.; Jin, X.; Wang, J.; Hu, Z.; Chen, C.-Y.; Kurioka, T.; Llandro, J.; Gibbons, A.H.; Sone, M.; Hsu, Y.-J.; Okamoto, S.; Chang, T.-F.M. Enhancement of Photocatalytic Activity in BiFeO3 Nanoparticles through Electrical Polarization. *Adv. Energ. Sust. Res.* **2025**, *6*, 2400285, https://doi.org/10.1002/aesr.202400285.
19. Wu, J.; Mao, W.; Wu, Z.; Xu, X.; You, H.; Xue, A.X.; Jia, Y. Strong pyro-catalysis of pyroelectric $BiFeO_3$ nanoparticles under a room-temperature cold–hot alternation. *Nanoscale* **2016**, *8*, 7343-7350, https://doi.org/10.1039/c6nr00972g.
20. Mocherla, P.S.V.; Karthik, C.; Ubic, R.; Ramachandra Rao, M.S.; Sudakar, C. Tunable bandgap in $BiFeO_3$ nanoparticles: The role of microstrain and oxygen defects. *Appl. Phys. Lett.* **2013**, *103*, 022910, https://doi.org/10.1063/1.4813539.
21. Prince, M.H.; Aishi, T.M.; Zubair, M.A.; Fakhrul, T. Tuning of the Structural, Optical and Magnetic Properties of $BiFeO_3$ Nanoparticles by Annealing. In Proceedings of the 2023 IEEE International Conference on Telecommunications and Photonics (ICTP), 21-23 Dec. 2023, Dhaka, Bangladesh; IEEE: **2023**; pp. 01-05, https://doi.org/10.1109/ictp60248.2023.10490725.
22. Masoudpanah, S.M.; Mirkazemi, S.M. Structural, Magnetic and Photocatalytic Properties of BiFeO3 Nanoparticles. *J. Nanostruct.* **2017**, *7*, 183–188, https://doi.org/10.22052/jns.2017.03.003.
23. Patel, S.K.S.; Lee, J.-H.; Kim, M.-K.; Bhoi, B.; Kim, S.-K. Single-crystalline Gd-doped $BiFeO_3$ nanowires: *R3*c-to-*Pn*2_1a phase transition and enhancement in high-coercivity ferromagnetism. *J. Mater. Chem. C* **2018**, *6*, 526-534, https://doi.org/10.1039/c7tc05362b.
24. Guo, R.; Fang, L.; Dong, W.; Zheng, F.; Shen, M. Enhanced Photocatalytic Activity and Ferromagnetism in Gd Doped $BiFeO_3$ Nanoparticles. *J. Phys. Chem. C* **2010**, *114*, 21390-21396, https://doi.org/10.1021/jp104660a.
25. Vashisth, B.K.; Bangruwa, J.S.; Gairola, S.P.; Verma, V. Structural, dielectric, ferroelectric and magnetic properties of Gd doped $BiFeO_3$. *Integr. Ferroelectr.* **2018**, *194*, 21-27, https://doi.org/10.1080/10584587.2018.1514869.
26. B, P.R.; Cui, H.; M, C.S.; Vattikuti, S.V.P.; Suh, Y.; Park, S.-H. Influence of Gd doping on the visible-light photocatalytic activity and magnetic properties of $BiFeO_3$ particles. *Mater. Res. Express* **2019**, *6*, 115044, https://doi.org/10.1088/2053-1591/ab463d.
27. Zhang, N.; Chen, D.; Niu, F.; Wang, S.; Qin, L.; Huang, Y. Enhanced visible light photocatalytic activity of Gd-doped $BiFeO_3$ nanoparticles and mechanism insight. *Sci. Rep.* **2016**, *6*, 26467, https://doi.org/10.1038/srep26467.
28. Sindhu, T.; Ravichandran, A.T.; Xavier, A.R.; Kumaresavanji, M. Structural, surface morphological and magnetic properties of Gd-doped $BiFeO_3$ nanomaterials synthesised by EA chelated solution combustion method. *Appl. Phys. A* **2023**, *129*, 685, https://doi.org/10.1007/s00339-023-06951-0.

29. Gyulakhmedov, R.R.; Faradzhev, S.P.; Khrustalev, A.N.; Sobola, D.; Sadykov, S.A.; Abdurakhmanov, M.G.; Abdulvakhidov, K.G.; Rabadanov, K.S.; Orudzhev, F.F.; Alikhanov, N.M.R. Ac-conductivity and structural, magnetic, dielectric, and photocatalytic properties of Gd doped $BiFeO_3$ nanoparticles. *J. Mater. Chem. C* **2025**, *13*, 19037-19054, https://doi.org/10.1039/d5tc01606a.
30. Liu, X.; Chao, J.; Guo, F.; Chang, L.; Zhang, X.; Long, W.; Xi, Z. Gd and Zr Co-Doped $BiFeO_3$ Magnetic Nanoparticles for Piezo-Photocatalytic Degradation of Ofloxacin. *Nanomaterials* **2025**, *15*, 792, https://doi.org/10.3390/nano15110792.
31. Khassaf, H.; Ibanescu, G.A.; Pintilie, I.; Misirlioglu, I.B.; Pintilie, L. Potential barrier increase due to Gd doping of $BiFeO_3$ layers in Nb:$SrTiO_3$-$BiFeO_3$-Pt structures displaying diode-like behavior. *Appl. Phys. Lett.* **2012**, *100*, 252903, https://doi.org/10.1063/1.4729816.
32. Jena, S.; Patra, S.K.; Singh, B.; Priyam, A.; Bhushan, B. Effect of Gd-doping on magnetic, ferroelectric, and optical properties of $BiFeO_3$ multiferroic nanoparticles synthesized by Sol-gel route. *Appl. Phys. A* **2025**, *131*, 503, https://doi.org/10.1007/s00339-025-08621-9.
33. Kim, J.W.; Do, D.; Kim, S.S.; Lee, M.H.; Sung, Y.S.; Kim, M.H.; Song, T.K. Effects of (Gd,Mn)-doping on ferroelectric properties of BiFeO3 thin films prepared using chemical solution deposition. In Proceedings of the 2011 International Symposium on Applications of Ferroelectrics (ISAF/PFM) and 2011 International Symposium on Piezoresponse Force Microscopy and Nanoscale Phenomena in Polar Materials, Vancouver, BC, Canada, 24-27 July 2011; IEEE: **2011**; pp. 1-4, https://doi.org/10.1109/isaf.2011.6014144.
34. Hossain, M.N.; Matin, M.A.; Rhaman, M.M.; Ali, M.A.; Hakim, M.A.; Roy, S.K. Structural and Dielectric Progression of 5 % Gd Doped $BiFeO_3$ Nanoparticles Through Cr (2-8%) Doping. *J. Eng. Sci.* **2022**, *12*, 101-110, https://doi.org/10.3329/jes.v12i3.57483.
35. B, P.R.; Park, S.H. Improved photocatalytic activity of $BiFeO_3$ nanoparticles upon Gd doping. *AIP Conf. Proc.* **2019**, *2087*, 020001, https://doi.org/10.1063/1.5095217.
36. Thang, D.V.; Hung, N.M. Effect of (Gd, Co) Co-Doping on Ferroelectric and Ferromagnetic Properties of $BiFeO_3$ Material. *ECS J. Solid State Sci. Technol.* **2025**, *14*, 053002, https://doi.org/10.1149/2162-8777/adcc52.
37. Shakir, I. Synthesis of Gd doped $BiFeO_3$/g-C_3N_4 composite: Enhancement of solar mediated photocatalytic performance. *Mater. Sci. Eng. B* **2024**, *302*, 117252, https://doi.org/10.1016/j.mseb.2024.117252.
38. Iqbal, S.; Bibi, F.; Farouk Elsadek, M.; Al-Mohaimeed, A.M.; Kalsoom, A.; Mahmood, M.; Tahir, A.A.; Jamshaid, M. Gd and Ni co-doped $BiFeO_3$ ferrite/r-GO nanocomposite for photocatalytic environmental remediation applications. *Mater. Sci. Semicond. Process.* **2024**, *179*, 108529, https://doi.org/10.1016/j.mssp.2024.108529.
39. Li, Z.; Dai, W.; Bai, L.; Wang, Y.; Ma, D.; Peng, Y.; Deng, Z.; Xie, Y.; Liu, B.; Zhang, G.; Wang, X.; Zhu, L. Gd-doped $BiFeO_3$ crystalline nanofibers for efficient rhodamine B in wastewater removal under simulated sunlight. *J. Alloys Compd.* **2023**, *968*, 171863, https://doi.org/10.1016/j.jallcom.2023.171863.
40. Anilkumar Singh, S.; Basantakumar Sharma, H. Analysis of structural and optical properties in co doped Mn,Gd in bismuth ferrite ($BiFeO_3$) thin films prepared by sol-gel technique. *Mater. Today Proc.* **2023**, https://doi.org/10.1016/j.matpr.2023.06.466.
41. Sharma, A.D.; Basantakumar Sharma, H. Structural, optical, and dispersive parameters of (Gd, Mn) co-doped $BiFeO_3$ thin film. *Mater. Today Proc.* **2022**, *65*, 2837-2843, https://doi.org/10.1016/j.matpr.2022.06.274.
42. Rizwan, S.; Awan, S.U.; Irfan, S. Room-temperature ferromagnetism in Gd and Sn co-doped bismuth ferrite nanoparticles and co-doped $BiFeO_3$/MXene (Ti_3C_2) nanohybrids for spintronics applications. *Ceram. Int.* **2020**, *46*, 29011-29021, https://doi.org/10.1016/j.ceramint.2020.08.072.
43. Utami, M.; Rahmah, A.; Andriyanti, W.; Istiqomah, N.I.; Kartika, B.M.; Wafi, A.; Insani, A.; Purwanto, S.; Suharyadi, E. Fabrication of rare earth Gd and Ce modified multiferroic $BiFeO_3$ for photocatalytic degradation of ibuprofen. *Results Chem.* **2025**, *18*, 102766, https://doi.org/10.1016/j.rechem.2025.102766.
44. Gupta, S.; Feng, L.J.; Medwal, R.; Vas, J.V.; Mishra, M.; Deen, G.R.; Paul, L.C.K.; Rawat, R.S. Spin-casted (Gd–Zn) co-doped $BiFeO_3$ thin films for sustainable oxide-electronics. *Mater. Sci. Semicond. Process.* **2021**, *132*, 105902, https://doi.org/10.1016/j.mssp.2021.105902.
45. Lotey, G.S.; Verma, N.K. Gd-doped $BiFeO_3$ nanoparticles – A novel material for highly efficient dye-sensitized solar cells. *hem. Phys. Lett.* **2013**, *574*, 71-77, https://doi.org/10.1016/j.cplett.2013.04.046.
46. Kiani, M.; Kiani, A.B.; Khan, S.A.; Rehmana, S.u.; Khan, Q.U.; Mahmood, I.; Saleemi, A.S.; Jalil, A.; Sohail, M.; Zhu, L. Facile synthesis of Gd and Sn co-doped $BiFeO_3$ supported on nitrogen doped graphene

for enhanced photocatalytic activity. *J. Phys. Chem. Solids* **2019**, *130*, 222-229, https://doi.org/10.1016/j.jpcs.2019.01.032.
47. Mai Oanh, L.T.; Thang, D.V.; Bich, D.D.; Chung, P.D.; Hung, N.M.; Van Quang, N.; Van Minh, N. Enhancement of ferroelectric and ferromagnetic properties of Gadolinium (Gd) and Nickel (Ni) co-doped $BiFeO_3$. *Ceram. Int.* **2020**, *46*, 17423-17429, https://doi.org/10.1016/j.ceramint.2020.04.036.
48. Basith, M.A.; Billah, A.; Jalil, M.A.; Yesmin, N.; Sakib, M.A.; Ashik, E.K.; Hoque Yousuf, S.M.E.; Chowdhury, S.S.; Hossain, M.S.; Firoz, S.H.; Ahmmad, B. The 10% Gd and Ti co-doped $BiFeO_3$: A promising multiferroic material. *J. Alloys Compd.* **2017**, *694*, 792-799, https://doi.org/10.1016/j.jallcom.2016.10.018.
49. Kumar, K.S.; Ramu, S.; Sudharani, A.; Ramanadha, M.; Murali, G.; Vijayalakshmi, R.P. Enhanced magnetic and dielectric properties of Gd doped $BiFeO_3$: Er nanoparticles synthesized by sol-gel technique. *Phys. E: Low-Dimens. Syst. Nanostructures* **2020**, *115*, 113689, https://doi.org/10.1016/j.physe.2019.113689.
50. Chai, Z.; Tan, G.; Yue, Z.; Yang, W.; Guo, M.; Ren, H.; Xia, A.; Xue, M.; Liu, Y.; Lv, L.; Liu, Y. Ferroelectric properties of $BiFeO_3$ thin films by Sr/Gd/Mn/Co multi-doping. *J. Alloys Compd.* **2018**, *746*, 677-687, https://doi.org/10.1016/j.jallcom.2018.02.352.
51. Godara, P.; Agarwal, A.; Ahlawat, N.; Sanghi, S. Crystal structure, dielectric and magnetic properties of Gd doped $BiFeO_3$ multiferroics. *Phys. B: Condens. Matter* **2018**, *550*, 414-419, https://doi.org/10.1016/j.physb.2018.08.045.
52. Mukherjee, A.; Basu, S.; Manna, P.K.; Yusuf, S.M.; Pal, M. Enhancement of multiferroic properties of nanocrystalline $BiFeO_3$ powder by Gd-doping. *J. Alloys Compd.* **2014**, *598*, 142-150, https://doi.org/10.1016/j.jallcom.2014.01.245.
53. Ablat, A.; Wu, R.; Mamat, M.; Li, J.; Muhemmed, E.; Si, C.; Wu, R.; Wang, J.; Qian, H.; Ibrahim, K. Structural analysis and magnetic properties of Gd doped BiFeO3 ceramics. *Ceram. Int.* **2014**, *40*, 14083-14089, https://doi.org/10.1016/j.ceramint.2014.05.137.
54. Suresh, P.; Babu, P.D.; Srinath, S. Role of (La, Gd) co-doping on the enhanced dielectric and magnetic properties of $BiFeO_3$ ceramics. *Ceram. Int.* **2016**, *42*, 4176-4184, https://doi.org/10.1016/j.ceramint.2015.11.091.
55. Chen, P.-Y.; Chen, C.-S.; Chiang, Y.-S.; Jou, Y.-S.; Chien, R.R.; Schmidt, V.H.; Tu, C.-S. Self-driven near-UV and visible light detection based on ITO/Gd-doped $BiFeO_3$/Au heterostructure. *J. Eur. Ceram. Soc.* **2021**, *41*, 5230-5239, https://doi.org/10.1016/j.jeurceramsoc.2021.04.010.
56. Vishwakarma, A.K.; Tripathi, P.; Srivastava, A.; Sinha, A.S.K.; Srivastava, O.N. Band gap engineering of Gd and Co doped $BiFeO_3$ and their application in hydrogen production through photoelectrochemical route. *nt. J. Hydrog. Energy* **2017**, *42*, 22677-22686, https://doi.org/10.1016/j.ijhydene.2017.07.153.
57. Mahesh, R.; Venugopal Reddy, P. A study of ferroelectric and magnetic properties of rare earth (RE=La, Nd, Sm, Gd) doped $BiFeO_3$ using modified Becke Johnson potential with SOC techniques. *Mater. Chem. Phys.* **2019**, *232*, 460-470, https://doi.org/10.1016/j.matchemphys.2019.05.012.
58. Kumar, A.; Yadav, K.L.; Kumar, S.; Kumar, N.; Mishra, A.; Kumar, N.; Shankar, U.; Mehrotra, T.; Sharma, G.; Kumar, R.; Adhikary, G.D. Magnetic, ferroelectric, and magnetodielectric properties of $BiFeO_3$ ceramic co-doped with Eu and Gd. *J. Phys. Chem. Solids* **2019**, *124*, 19-23, https://doi.org/10.1016/j.jpcs.2018.08.037.
59. Kim, Y.-J.; Kim, J.W.; Raghavan, C.M.; Oak, J.-J.; Kim, H.J.; Kim, W.-J.; Kim, M.H.; Song, T.K.; Kim, S.S. Enhancement of electrical properties of (Gd, V) co-doped $BiFeO_3$ thin films prepared by chemical solution deposition. *Ceram. Int.* **2013**, *39*, S195-S199, https://doi.org/10.1016/j.ceramint.2012.10.061.
60. Pradhan, S.K.; Roul, B.K. Effect of Gd doping on structural, electrical and magnetic properties of $BiFeO_3$ electroceramic. *J. Phys. Chem. Solids* **2011**, *72*, 1180-1187, https://doi.org/10.1016/j.jpcs.2011.07.017.
61. Mallick, P.; Kumari Yadav, S.; Satpathy, S.K.; Behera, B.; Moharana, S.; Sagadevan, S. Impact of gadolinium doping on $BiFeO_3$-$PbZrO_3$ for energy storage applications: Structural, microstructural, and thermistor properties. *Inorg. Chem. Commun.* **2024**, *166*, 112626, https://doi.org/10.1016/j.inoche.2024.112626.
62. Pradhan, S.K.; Das, J.; Rout, P.P.; Das, S.K.; Mishra, D.K.; Sahu, D.R.; Pradhan, A.K.; Srinivasu, V.V.; Nayak, B.B.; Verma, S.; Roul, B.K. Defect driven multiferroicity in Gd doped $BiFeO_3$ at room temperature. *J. Magn. Magn. Mater.* **2010**, *322*, 3614-3622, https://doi.org/10.1016/j.jmmm.2010.07.001.
63. Chauhan, S.K.; Kumar, A.; Verma, N.K.; Jena, P.; Mahanti, B.; Singh Patel, S.K. *R3c* to *P1* phase transition in Nd^{3+}/Gd^{3+} co-doped $BiFeO_3$ nanoparticles: Enhanced magnetic and photocatalytic properties. *Mater. Sci. Eng., B* **2025**, *317*, 118170, https://doi.org/10.1016/j.mseb.2025.118170.

64. Rai, R.; Bdikin, I.; Valente, M.A.; Kholkin, A.L. Ferroelectric and ferromagnetic properties of Gd-doped $BiFeO_3$–$BaTiO_3$ solid solution. *Mater. Chem. Phys.* **2010**, *119*, 539-545, https://doi.org/10.1016/j.matchemphys.2009.10.011.
65. Batoo, K.M.; Ijaz, M.F.; Imran, A.; Pandiaraj, S. Duple charge separation and plasmonically enriched DSSC and piezo-photocatalytic efficacy of Au anchored perovskite Gd^{3+}:$BiFeO_3$ nanospheres. *Chemosphere* **2024**, *346*, 140410, https://doi.org/10.1016/j.chemosphere.2023.140410.
66. Mallikarjuna, A.; Ramesh, S.; Kumar, N.S.; Babu Naidu, K.C.; Ratnam, K.V.; Manjunatha, H.; Rao, B.P. Structural transformation and high negative dielectric constant behavior in (1-x) ($Al_{0·2}La_{0·8}TiO_3$) + (x) ($BiFeO_3$) (x = 0.2–0.8) nanocomposites. *Phys. E: Low-Dimens. Syst. Nanostructures* **2020**, *122*, 114204, https://doi.org/10.1016/j.physe.2020.114204.
67. Venkata Shiva Reddy, B.; Srinivas, K.; Suresh Kumar, N.; Chandra Babu Naidu, K.; Ramesh, S. Nanorods like microstructure, photocatalytic activity and ac-electrical properties of (1-x) ($Al_{0.2}La_{0.8}TiO_3$) + (x) ($BaTiO_3$) (x = 0.2, 0.4, 0.6 & 0.8) nanocomposites. *Chem. Phys. Lett.* **2020**, *752*, 137552, https://doi.org/10.1016/j.cplett.2020.137552.
68. Sahu, S.; Mohapatra, P.P.; Karnajit Singh, H.; Dobbidi, P. Enhanced microwave absorbing performance of Sr^{2+} substituted Nickel-Cobalt nano ferrite for radar and stealth applications. *Mater. Sci. Eng., B* **2023**, *294*, 116514, https://doi.org/10.1016/j.mseb.2023.116514.
69. Shannon, R.D. Revised effective ionic radii and systematic studies of interatomic distances in halides and chalcogenides. *Acta Crystallogr. A* **1976**, *32*, 751–767, https://doi.org/10.1107/s0567739476001551.
70. Scherrer, P. Bestimmung der Größe und der inneren Struktur von Kolloidteilchen mittels Röntgenstrahlen. *Nachrichten von Der Gesellschaft Der Wissenschaften Zu Göttingen, Math. Klasse* **1918**, *1918*, 98-100.
71. Dastagiri, S.; Lakshmaiah, M.V.; Chandra Babu Naidu, K.; Suresh Kumar, N.; Khan, A. Induced dielectric behavior in high dense $Al_xLa_{1-x}TiO_3$ (x = 0.2–0.8) nanospheres. *J. Mater. Sci. Mater. Electron.* **2019**, *30*, 20253-20264, https://doi.org/10.1007/s10854-019-02409-3.
72. Dastagiri, S.; Pakardin, G.; Babu, T.A.; Lakshmaiah, M.V.; Naidu, K.C.B. Colossal dielectric behavior in $Al_{0.8}Gd_yLa_{0.2-y}TiO_3$ (y = 0.01–0.04) nanostructures. *J. Mater. Sci. Mater. Electron.* **2021**, *32*, 8017-8032, https://doi.org/10.1007/s10854-021-05525-1.
73. Dastagiri, S.; Lakshmaiah, M.V.; Chandra Babu Naidu, K. Defect dipole polarization mechanism in low-dimensional europium substituted $Al_{0.8}La_{0.2}TiO_3$ nanostructures. *Phys. E: Low-Dimens. Syst. Nanostructures* **2020**, *120*, 114058, https://doi.org/10.1016/j.physe.2020.114058.
74. Naidu, K.C.B.; Kumar, N.S.; Banerjee, P.; Reddy, B.V.S. A review on the origin of nanofibers/nanorods structures and applications. *J. Mater. Sci.: Mater. Med.* **2021**, *32*, 68, https://doi.org/10.1007/s10856-021-06541-7.
75. Kadiyala, C.B.N.; Wuppulluri, M. Effect of microwave heat treatment on pure phase formation of hydrothermal synthesized nano NiMg ferrites. *Ph. Transit.* **2017**, *90*, 847-862, https://doi.org/10.1080/01411594.2016.1277220.
76. Lu, L.; Li, J.; Yu, J.; Song, P.; Ng, D.H.L. A hierarchically porous $MgFe_2O_4$/γ-Fe_2O_3 magnetic microspheres for efficient removals of dye and pharmaceutical from water. *Chem. Eng. J.* **2016**, *283*, 524-534, https://doi.org/10.1016/j.cej.2015.07.081.
77. Yellanna, M.; Naidu, K.C.B.; Kumar, N.S.; Devi, D.M.; Kumari, P.A. Magneto-dielectric and thermal study of Gd-doped nano nickelates. *J. Mater. Sci. Mater. Electron.* **2023**, *34*, 2307, https://doi.org/10.1007/s10854-023-11741-8.
78. Machakanti, Y.; Chandra Babu Naidu, K.; D, B.B.; Madunuri, C.; N, S.K.; A, R.; Khan, A. Low-temperature hydrothermal synthesis of $NiEuFe_2O_4$ nanoparticles: Magnetic, thermal, and magneto-dielectric behavior. *Int. J. Appl. Ceram. Technol.* **2024**, *21*, 715-726, https://doi.org/10.1111/ijac.14574.
79. Sagar, T.V.; Rao, T.S.; Naidu, K.C.B. Effect of calcination temperature on optical, magnetic and dielectric properties of Sol-Gel synthesized $Ni_{0.2}Mg_{0.8-x}Zn_xFe_2O_4$ (x = 0.0–0.8). *Ceram. Int.* **2020**, *46*, 11515-11529, https://doi.org/10.1016/j.ceramint.2020.01.178.
80. Jiang, Y.; Sun, A.; Huang, X.; Wang, J.; Zhang, Y.; Shao, L. Influence of Bi^{3+} ions doping on the structure and magnetic properties of Cu-Co nanoferrite. *J. Mater. Sci. Mater. Electron.* **2021**, *32*, 27882-27898, https://doi.org/10.1007/s10854-021-07170-0.
81. Kumari, P.A.; Devi, D.M.; Chandrasekhar, M.; Kumar, N.S.V. Structure, Dielectric, and Thermal Behavior of Bismuth Titanate Nanoparticles. *ChemistrySelect* **2025**, *10*, e202404134, https://doi.org/10.1002/slct.202404134.

82. Rajender, T.; Naidu, K.C.B.; Basha, D.B.; Samanta, S.; Reddy, L.S.S. Magnetic, dielectric and thermal study of $CoNiFe_2O_4$ nanoparticles. *Nano-Struct. Nano-Objects* **2024**, *38*, 101167, https://doi.org/10.1016/j.nanoso.2024.101167.

Publisher's Note & Disclaimer